

## Numerical simulation and experimental validation of the large deformation bending and folding behavior of magneto-active elastomer composites

This content has been downloaded from IOPscience. Please scroll down to see the full text.

2014 Smart Mater. Struct. 23 094004

(<http://iopscience.iop.org/0964-1726/23/9/094004>)

View [the table of contents for this issue](#), or go to the [journal homepage](#) for more

Download details:

IP Address: 128.173.127.127

This content was downloaded on 31/08/2014 at 21:08

Please note that [terms and conditions apply](#).

# Numerical simulation and experimental validation of the large deformation bending and folding behavior of magneto-active elastomer composites

Robert Sheridan<sup>1</sup>, Juan Roche<sup>2</sup>, Samuel E Lofland<sup>2</sup> and Paris R vonLockette<sup>1</sup>

<sup>1</sup> Pennsylvania State University, 150B Hammond Bldg., University Park, PA 16802, USA

<sup>2</sup> Rowan University, Department of Physics, 201 Mulic Hill Road, Glassboro, NJ 08028, USA

E-mail: [prv2@psu.edu](mailto:prv2@psu.edu)

Received 16 May 2014, revised 27 June 2014

Accepted for publication 30 June 2014

Published 11 August 2014

## Abstract

This work seeks to provide a framework for the numerical simulation of magneto-active elastomer (MAE) composite structures for use in origami engineering applications. The emerging field of origami engineering employs folding techniques, an array of crease patterns traditionally on a single flat sheet of paper, to produce structures and devices that perform useful engineering operations. Effective means of numerical simulation offer an efficient way to optimize the crease patterns while coupling to the performance and behavior of the active material. The MAE materials used herein are comprised of nominally 30% v/v, 325 mesh barium hexaferrite particles embedded in Dow HS II silicone elastomer compound. These particulate composites are cured in a magnetic field to produce magneto-elastic solids with anisotropic magnetization, e.g. they have a preferred magnetic axis parallel to the curing axis. The deformed shape and/or blocked force characteristics of these MAEs are examined in three geometries: a monolithic cantilever as well as two- and four-segment composite accordion structures. In the accordion structures, patches of MAE material are bonded to a Gelest OE41 unfilled silicone elastomer substrate. Two methods of simulation, one using the Maxwell stress tensor applied as a traction boundary condition and another employing a minimum energy kinematic (MEK) model, are investigated. Both methods capture actuation due to magnetic torque mechanisms that dominate MAE behavior. Comparison with experimental data show good agreement with only a single adjustable parameter, either an effective constant magnetization of the MAE material in the finite element models (at small and moderate deformations) or an effective modulus in the minimum energy model. The four-segment finite element model was prone to numerical locking at large deformation. The effective magnetization and modulus values required are a fraction of the actual experimentally measured values which suggests a reduction in the amount of magnetic torque transferred from the particles to the matrix.

Keywords: origami engineering, magneto-active elastomers, finite element methods, magneto-rheological elastomers

## Introduction

Magneto-active elastomers (MAE) are a new branch of smart composites where ferromagnetic particles are embedded in an

elastomer matrix prior to the cross-linking process. This allows an otherwise inactive rubber to exhibit magneto-sensitive behaviors caused by inter-particle and particle-field interactions that produce actuation such as magneto-striction

[1], bending [2–5], and shearing [6, 7], which also increase the material's stiffness [5, 8, 9]. The magnitude and mode of the actuation is a function of the distribution and volume fraction of the magnetic particles, the magnitude and direction of the magnetic field, the geometry and boundary conditions of the MAE, and the material properties (such as the isotropy or anisotropy of the compliance or permeability). MAEs, arguably a class of their own, are not to be confused with magneto-rheological elastomers (MRE) as MREs are primarily driven by magnetic force (attraction) interactions between particles as opposed to MAEs being driven primarily by magnetic torques [3–7].

The magnetic particles (barium hexaferrite) used in this experiment are aligned during this production of the material to physically, and ideally, orient the particles in the direction of the applied magnetic field. This creates an anisotropic composite where the particle-field behavior is dependent on which direction the magnetic field is applied in relation to the orientation of the magnetic particles; a distributed magnetic torque  $\mathbf{T}$  is generated following  $\mathbf{T} = \mathbf{m} \times \mathbf{H}$ , where  $\mathbf{H}$  is the applied magnetic field and  $\mathbf{m}$  the remanent magnetization in the MAE material. This torque is aggregated across all particles to produce macroscopic response [3, 7]. The structures in this work use either solid MAE cantilevers or MAE specimens attached to a non-magnetic PDMS layer to create composite structures.

While this work examines actuation, other works have evaluated the magnetic shear and tensile stiffening response of materials comprised of soft-magnetic filler particles (MREs) with respect to the applied magnetic field [2, 8, 10–13]. For example, in [2], the MRE material demonstrated large shear stiffness increases under the application of magnetic fields which were applied with a 450 mT permanent magnet. The MRE also demonstrated high strain potential (approximately 20%) which makes it suitable for applications in which large deformations are required and magnetic work potential is also required. Other more recent works have studied the feasibility of using hard-magnetic MAE structures for actuation and to perform work [3–6]. These works have evaluated deformation and bend angles of the structures in relation to the applied field for defined geometries and force versus deflection curves for synthetic work calculations.

Further works have studied giant or colossal magneto-rheological effects. For example [14], deals with several issues including nonlinear magneto-optical Kerr effects in three dimensions and magneto-phonic responses for the manipulation of light propagation through conducting systems with dielectric islands or dielectric systems with metallic islands. The latter gives rise to the development of surface plasmon resonance which produces extraordinary light transmission through thin films [14]. Furthermore, in [15] colossal increases in the storage modulus of up to 10<sup>6</sup>% are recorded for soft-magnetic MAE materials.

An initial goal of origami engineering from an active-materials standpoint is to develop material systems (solid state compounds, polymer blends and compositions, composites, laminates, structures, etc) capable of folding, and

arguably unfolding, due to external stimuli. Previous works on MAEs showed that this has been achieved [3–6]. A logical next step is the ability to model the MAE materials in use. The development of useful computational models will allow researchers to develop and optimize more complicated origami structures. Such modeling, however is complicated by the elasto-magnetic coupling present in MAEs, their macroscopic-shape-dependent disturbance of local magnetic field, and, most importantly, their reliance primarily on magnetic torque response as opposed to magneto-strictive forces. To deal with these issues, this work investigates the use of the Maxwell surface stress (MSS) method in order to produce accurate predictive results. This is done by solving Maxwell's equations in parallel with the equations for conservation of momentum [6, 7, 16]. Actuation in the model is achieved through a distribution of Maxwell surface tractions, which are calculated via the change in Maxwell stresses at magnetic/non-magnetic material boundaries. This method varies from many existing models of MREs, theoretical and computational, that are driven by internal body forces that act on either embedded particles or point-wise through the material due to local field disturbances [17, 18].

Outside of magnetically-active materials, origami engineering has also been pertinent to the development of actuators that do not use the traditional mechanical components (e.g motors, bearings, etc). In [19], a paper-Ecoflex (silicone elastomer) composite is used to create various forms of actuation that include bending, linear contraction and extension, and twisting. The composite generates the aforementioned modes of actuation by incorporating anisotropy into the otherwise isotropic elastomeric polymers. The anisotropy is prevalent due to the presence of paper which is stiffer than the polymer, inextensible, yet still flexible [19]. The resulting composite can then be 'programmed' to have a predetermined mode of actuation. In [20], a sheet of conducting paper was folded using electro-active polymers (EAP). The actuation in [20] occurs due to electrically-induced changes in the elastic modulus of the polymer film which is humido-sensitive and conductive. This occurs through reversible sorption and desorption of water vapor molecules [20]. The structures actuated in [20] consisted of the paper crane and Miura-Ori but the principles can be applied to various structures.

In [21] and [22], researchers aimed to develop a folding actuator design capable of transforming a planar geometry into various three-dimensional shapes such as a paper airplane or boat structure. Actuation was achieved through a shape-memory alloy which allows bidirectional actuation. This allows the structures to both fold and unfold through use of the active material. Furthermore, the researchers used feedback control from pressure, strain, and curvature sensors to actuate the structures into intermediate positions; past studies only allowed the structures to fold into their two extreme positions (completely folded or completely unfolded). Highlights of the works include fabrication and quantitative characterization of the robotic structures.

### Modeling of magneto-elastic solids

There are several works in the literature that present systems of equations suitable for solutions to problems involving deformable magneto-elastic solids under magnetic and elastic loading. Notably [23] calculated the overall deformation and stress-strain relations using fully coupled magneto-elastic interactions. [24] summarized the equations governing deformation with particular reference to elastomers whose mechanical properties can change rapidly by the application of a magnetic field. [24] illustrated the magneto-elastic coupling phenomena, using both Lagrangian and Eulerian analyses, in a cylinder subjected to traction or torsion under the presence of external magnetic fields. Besides these models [26], and [27] have also proposed micro-mechanically based particulate composite concepts while [28] examines the problem using homogenization methods. It should be noted that recent work has begun to scrutinize assumptions of regularly ordered microstructures [29].

Although the aforementioned models provide important analytical frameworks to simulate magneto-elastic solid behavior, their solutions apply only to bodies of infinite extent and/or were derived for isotropic magneto-elastic materials. Recently [30–32] presented constitutive equations that govern the interaction between an anisotropic magneto-elastic solid and a magnetic field. [31, 32] study the role of particle shape anisotropy while [30] investigates an incompressible magneto-elastic anisotropic material capable of large deformations. These types of models are important because magnetic anisotropy drives magnetic torque-based actuation, beyond magneto-strictive shear stiffening effects. These models, though addressing anisotropy in the geometry of ferromagnetic inclusions or their arrangements, avoid *intrinsic* magnetic anisotropy of the inclusion (e.g. hard-magnetic behavior). Instead, actuation is driven by interaction of the anisotropic magnetization induced by geometry, and internal to the inclusion (or developed in an array of inclusions), with the externally applied fields, e.g. it is a result of geometrically induced local demagnetizing fields. This limits the classes of behavior which they can address by restricting analytical model predictions to soft-magnetic material behaviors. Specifically, bidirectional behavior, which can be generated through *magnetic* anisotropy between the ferromagnetic inclusions and the external field to generate magnetic torque, is beyond the scope of even these latter works.

For this reason, a number of actuation experiments on MAE's (e.g. materials with hard-magnetic filler particles) driven by a magnetic field exist to examine these effects. [3–5] showed the free deformation and force versus deformation behavior of various MAE cantilevers containing different ferrite compounds as the magnetic filler, proving reversibility and large deformation bending actuation as well as using beam theory to estimate a hypothetical internal moment. [29] highlighted the ability of hard-magnetic BaM MAEs to perform large deformation dynamic shearing actuation under the influence of an oscillatory transverse magnetic field.

Several works on developing formulations suitable for the numerical modeling of MRE/MAE materials exist in the

literature. These works take as their bases continuum mechanics formulations of the kinematics of the deforming matrix and rigid (and semi-rigid) inclusion, nonlinear elastic response of the matrix materials and linear elastic (or rigid) response of the inclusions, and, most importantly, free energy or constitutive formulations of the inclusion's response to the magnetic field [18, 33–35]. In some works the formulations explicitly state the use of isotropic or non-polar (i.e. soft-magnetic) magnetic constitutive or energy models [18, 34, 36] while in others the form of the free magnetic energy density is not given explicitly [37]. In [35], however, a form of the magnetic energy density suitable for hard-magnetic response is given, though, in that work, the formulation for possibly hard-magnetic behavior is not compared to data. [38] addresses the difficult problem of simulating the self-field local to the material while addressing soft-magnetic magneto-elastic thin films in two-dimensions. The numerical results given in these works are able to predict shear stiffening seen in soft-magnetic MREs in shear as well as magneto-elastic response for cylindrical and other standard geometries, but these formulations have not been validated against hard-magnetic MAE experimental response.

A problem of similar geometry (in an axisymmetric representation) to those studied herein was formulated in [42]. [42] examines the bulging instability of a thin circular plate of soft-magnetic film subjected to a transverse field and was able to numerically capture the bulging phenomena as well as calculate analytically the critical buckling field as a function of geometry and material parameters, showing good agreement with data. The numerical results in [42] were based on the governing equations and subsequent finite element formulation detailed in [43]. The analytical results used small strain and deformation theory as well as linear elasticity; the material was also assumed soft-magnetic. The numerical results also assumed small strains, linear elasticity, and soft-magnetic behavior. Of most interest were the magneto-elastic coupling equations generated as traction boundary conditions on the system, e.g. equation (6) in [43] which equated a magnetically induced traction to the mechanical traction on the boundary between magnetic and non-magnetic domains. Though the formulation and results of [42, 43] are valid for soft-magnetic materials in the linear elastic regime, and are therefore not directly comparable to the current work, they suggest that exploration of the use of transitions of the Maxwell stress between magnetic and non-magnetic domains as a surface traction for modeling hard magnetic materials is warranted.

The objective of this work was to develop a predictive modeling framework for MAE behavior for hard-magnetic MAEs and validate it by comparison to data in multiple geometries. This was accomplished by developing multi-physics computational models with COMSOL, a commercial finite element package, using a set of effective bulk properties and employing the MSS to couple the elastic and magnetic behaviors. The results of the simulation were then compared to simulation results on MAEs having three geometries: a monolithic MAE cantilever, a two-segment accordion MAE-PDMS composite and a four-segment accordion MAE-PDMS composite.

**Table 1.** Dimensions of the MAE cantilevered beam, the two-segment accordion structure, and the four-segment accordion structure.

|                       | Cantilever beam | Two-segment accordion, prime | Four-segment accordion, double prime |
|-----------------------|-----------------|------------------------------|--------------------------------------|
| Dimensional parameter | Value (mm)      | Value (mm)                   | Value (mm)                           |
| MAE thickness (A)     | 20.0            | 4.85                         | 15.0                                 |
| MAE height (B)        | 5.0             | 3.1                          | 3.18                                 |
| MAE length (C)        | 50.0            | 10.0                         | 20.3                                 |
| MAE spacing (D)       | 25.0            | 10.0                         | 9.53                                 |
| PDMS thickness (E)    | —               | 4.85                         | 15.0                                 |
| PDMS height (F)       | —               | 2.8                          | 3.18                                 |
| PDMS length (G)       | —               | 52.0                         | 119.0                                |
| Offset (H)            | —               | 10.0                         | —                                    |

## Experimental methods

### Materials and composite fabrication

The MAE material used consisted of DOW HS II RTV silicon rubber mixed at 20:1 base to catalyst ratio. Barium hexaferrite (325 mesh) was mixed into the silicon rubber at a 30% v/v prior to curing. Acrylic molds were used to cast the specimens into sheets. The closed molds were rectangular with prescribed dimensions to create specimens detailed in table 1. MAEs were magnetically aligned by subjecting the specimens to a  $\sim 2$  Tesla magnetic field. Samples were either magnetized in plane or out of plane. A similar casting procedure was used with the PDMS materials. The PDMS substrate was created with Gelest OE 41 a two-part compound mixed 1:1 by weight. This compound was also cast in rectangular molds of desired thickness and allowed to cure producing sheets from which desired cross sections either used as cast or cut to the desired shape.

For the two-segment and four-segment MAE accordion structures, the MAE segments were bonded to the PDMS substrate with Loctite's Plastic Bonding System two-part adhesive. This adhesive was suitable for elastomer on elastomer bonding. The magnetizations of the in-plane MAEs bonded to the PDMS substrate were oriented in opposite directions to induce mountain or valley folds between the MAE segments for the two-segment and four-segment accordion structures (see figures 1(B) and (C)), respectively. The poling in the out-of-plane MAE cantilever was nominally uniform (see figure 1(A)) and transverse to the beam axis.

### Experimental methods

Results of experiments on the three distinct geometries (see figure 1) were used for comparison to simulations. In each case loading and displacement boundary conditions varied, as detailed in the figure and discussed below.

**Cantilever bending.** In a prior work, the cantilever bending behavior of hard- magnetic MAE samples was examined. Samples were fabricated as discussed previously. Details of sample preparation can be found in [3].

A schematic of the force-deflection test setup is shown in figure 2. The MAE samples were fixed at the base leaving 50 mm free length and  $20 \times 5 \text{ mm}^2$  cross section. Resulting cantilevers were subjected to increasing magnetic field strengths up to  $\mu_0 H \sim 0.09 \text{ T}$  in order to study the dependence of magnetic field strength and tip deflection on reaction force,  $F$ . Details of the experimental setup can be found in [3].

### Two- and four-segment accordion geometry and experiment.

The accordion structures were placed between the pole faces of a C-shape electromagnet such that the magnetic field and magnetization of the MAEs were perpendicular to each other (figures 3 and 4). The two-segment accordion structure was fixed on the upper portion of the PDMS substrate and attached to a Shimpo force gauge (Model FGV-0.5XY with an accuracy of  $\pm 0.1\%$ ) on the bottom portion of the PDMS. A view of the actuated experimental set-up can be seen in figure 3(c). The experiment recorded the axial force applied by the MAE accordion structure to the Shimpo force gauge as the magnetic field was increased in increments of  $\sim 10 \text{ mT}$ . For the four-segment structure, the PDMS substrate was fixed at the top, only. In either case, a high-resolution Canon EOS 7D camera ( $5184 \times 3456$  pixels) was used to photograph the deformed specimen and the bend angles were measured with AutoCAD software. The two-segment structure was tested for this work while experimental results for the four-segment structure were initially reported in [6].

## Finite element modeling

### Problem formulation

Finite element analysis (FEA) of the cantilevered beam, two-segmented, and four-segmented MAE accordion structures was performed with Comsol Multiphysics [16] in two-dimensions. Note that the resulting system of equations is solved in a mixed Eulerian–Lagrangian formulation and uses finite deformation kinematics to account for expected large deformation; the software also periodically re-meshes the geometry to remove regions containing distorted elements. Details of the numerical procedures may be found in [16]; this section seeks to highlight the methods used, e.g. model geometry, governing equations, constitutive laws, and boundary conditions, which are discussed in a Lagrangian description for simplicity.



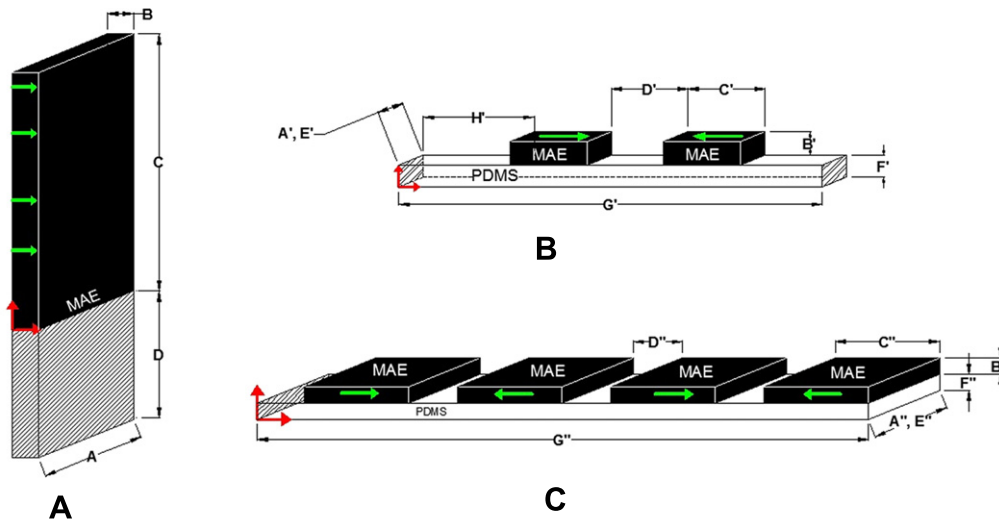


**Figure 1.** Depicts the dimensions and boundary conditions for the MAE cantilevered beam (A), two-segment accordion structure (B), and four-segment accordion structure (C). The red arrows denote the horizontal and vertical axes for the  $x$ -axis and  $y$ -axis, respectively. The green arrows depict the direction of remanent magnetization in the MAE specimens. The hatched areas depict fixed boundary conditions. The letters used to denote dimensions are described in detail in table 1.

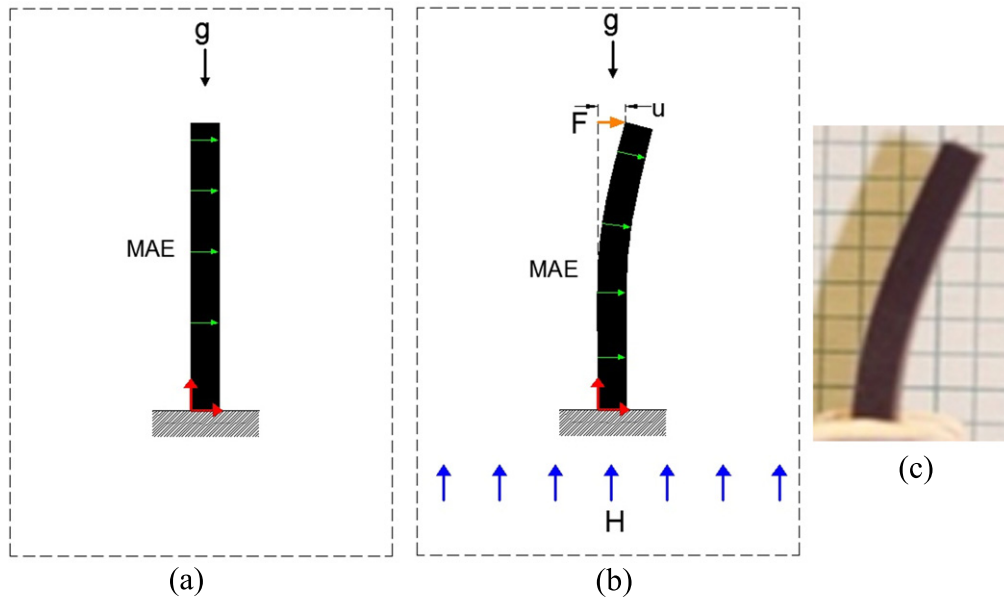


**Figure 2.** (a) Schematic of the undeformed shape (b) schematic of measurements on deformed shape, (c) image of representative deformed shape for the cantilever geometry.

The domains for the cantilevered beam modeled can be seen in figure 2(a) which consists of an MAE beam and an air box. The air box is bounded by the dotted line at the outer boundary of the figure. A continuity condition exists in the magnetic field variables across the air-MAE boundary. As seen in figure 2(a), the MAE domain is subjected to a fixed boundary condition on the bottom boundary of the beam. The upper boundary of the beam is subjected to a proscribed  $x$ -displacement condition; the  $x$ -component of the total reaction force along this boundary is then compared to the experimental tip force. The domains for the two-segmented accordion can be seen in figure 3(a) and consist of two MAE segments, a PDMS substrate, and an air domain. As seen in

figure 3(a), the substrate is subjected to fixed boundary conditions on the upper and lower boundaries. The  $y$ -component of the total reaction force on the boundary is compared to the experimental force measurement. The MAE patches are fixed to the substrate (continuity condition in displacements and magnetic field) while the entire structure is contained within an air domain (continuity in magnetic field only). The domains for the four-segmented accordion can be seen in figure 4(a) and consist of four MAE segments, a PDMS substrate, and an air box. The substrate is fixed at the top and free on the bottom. In each model, gravity acts downward. The air domains are necessary to accurately model the driving magnetic field.

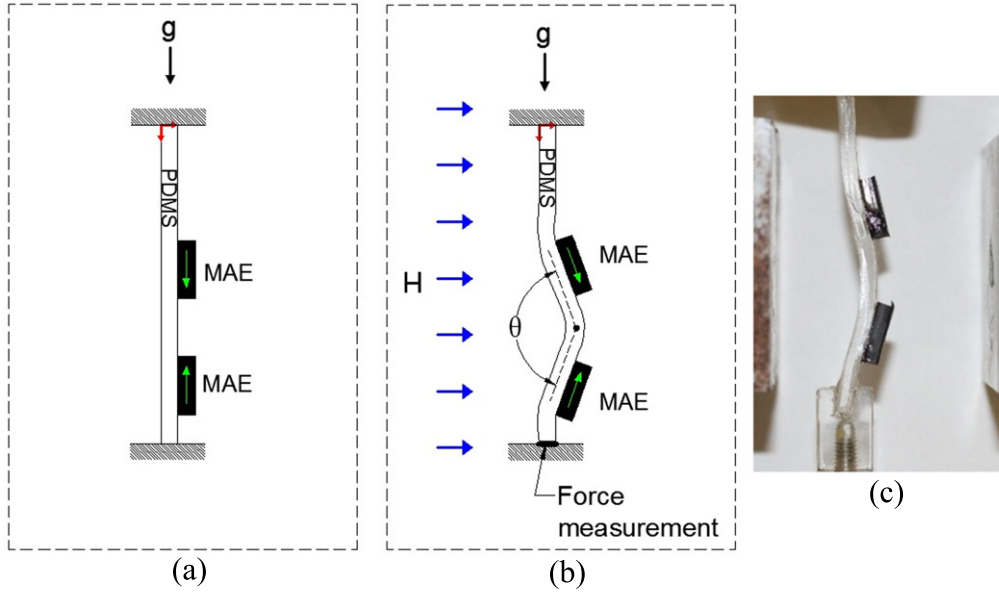


**Figure 3.** (a) Schematic of undeformed shape (b) measurement of fold angle and (c) image of representative deformed shape. The surrounding box in (a) and (b) display the extent of the air domain used in the finite element model.

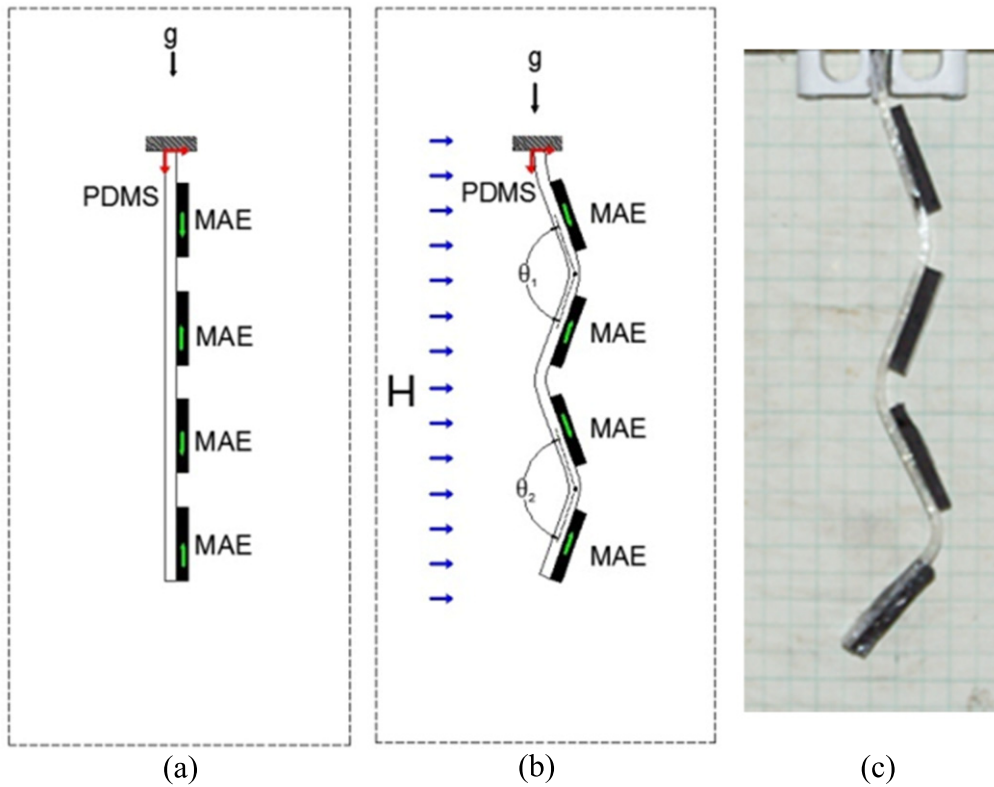


**Figure 4.** (a) Schematic of undeformed shape (b) schematic showing measurements of two mountain-fold bend angles which are then averaged and (c) image of representative deformed shape.

**Governing differential equations.** The finite element model in this paper uses a method which applies a mechanical traction through the MSS tensor along the boundary between the magnetic and non-magnetic domains to actuate the structure [16]. The MSS is the application of the Maxwell Stress calculated as a traction along a surface between magnetic and non-magnetic domains. This method seeks to solve static

conservation of moment in parallel with Maxwell's equations for magneto-statics, namely,

$$\nabla \cdot \sigma = 0, \quad (1a)$$

$$\nabla \times \mathbf{H} = 0, \quad (1b)$$

$$\nabla \cdot \mathbf{B} = 0, \quad (1c) \quad \mathbf{C}_E, \text{ which is defined as}$$

where  $\boldsymbol{\sigma}$  is the Cauchy stress and  $\mathbf{B}$  the magnetic induction.

*Constitutive and kinematic equations.* The magnetic behavior of the MAE, substrate and air domains is given as

$$\mathbf{B} = \mu_0 \mathbf{H} + \mathbf{M}, \quad (2)$$

where  $\mathbf{M}$  is the magnetization of the domain and  $\mu_0 = 1.257 \text{ N A}^{-2}$  is the permeability of free space. For the substrate and the air domains,  $\mathbf{M} = 0$ . Note that  $\mathbf{M}$  is considered in an Eulerian frame and thus follows the structure's deformed geometry.

The elastic behavior of the PDMS substrate was assumed to follow the Mooney–Rivlin solid model since many elastomers can be modeled accurately by fitting the model constants to experimental data [33, 34]. The Mooney–Rivlin strain energy density linearly combines invariants of the left Cauchy–Green deformation (stretch) tensor  $\mathbf{B}_E$  (not to be confused with the magnetic induction  $\mathbf{B}$ ) where the strain energy density  $U$  is defined as

$$U = C_{10}(\bar{I}_1 + 3) + C_{01}(\bar{I}_2 + 3) + \frac{K_1}{2}(J - 1)^2, \quad (3)$$

where  $C_{10}$ ,  $C_{01}$ , and the bulk modulus,  $K_1$ , are material properties,  $\mathbf{J}$  is the Jacobian matrix, and  $\bar{I}_1$  and  $\bar{I}_2$  are the first and second invariants of the deviatoric component of the Cauchy–Green deformation tensor, respectively [34]. The incompressibility of the material implies that there is no net volume change during deformation (i.e.  $\mathbf{J} = 1$ ). This is modeled internally in Comsol by modifying the second Piola–Kirchoff stress tensor to remove the effect of volumetric strain from the original stress tensor but adds additional constraints [16]. The stress-strain relation as a Mooney–Rivlin solid can then be calculated from the strain energy density as

$$\sigma_{ij} = \frac{\mu_1}{J^{5/3}} \left( B_{ij} - \frac{1}{3} B_{kk} \delta_{ij} \right) + \frac{\mu_2}{J^{7/3}} \left( B_{kk} B_{ij} - \frac{1}{3} [B_{kk}]^2 \delta_{ij} - B_{ik} B_{kj} + \frac{1}{3} B_{kn} B_{nk} \delta_{ij} \right), \quad (4)$$

where

$$B_{ij} = \lambda_1^2 b_i^{(1)} b_j^{(1)} + \lambda_2^2 b_i^{(2)} b_j^{(2)} + \lambda_3^2 b_i^{(3)} b_j^{(3)}. \quad (5)$$

$\delta_{ij}$  is the Kronecker delta, and  $\lambda_{1/2/3}$  and  $b_{i/j}$  are eigenvalues and eigenvectors of the deformation tensor, respectively. The left Cauchy–Green deformation tensor is related to the deformation gradient  $\mathbf{F}$  through

$$\mathbf{B}_E = \mathbf{F} \cdot \mathbf{F}^T \quad (6a)$$

allowing solution for the displacement field  $\mathbf{u} = [u, v, w]^T$  where  $u, v$  and  $w$ , are the component displacements from equations (1a), (3)–(6a), and appropriate boundary conditions in terms of mechanical equilibrium. Note that the strain field,  $\mathbf{E}$ , can be calculated by using the right Cauchy–Green tensor,

$$\mathbf{C}_E = \mathbf{F}^T \cdot \mathbf{F} \quad (6b)$$

from which the strain can be calculated through

$$\mathbf{E} = \frac{1}{2}(\mathbf{C}_E - \mathbf{I}). \quad (6c)$$

*3.1.3. MSS.* The elastic and magnetic responses of the MAE are coupled through the MSS. Modeling with the MSS method aims to solve (1a)–(1c) concurrently, given magnetic and elastic material behaviors as defined by (2) and (3), respectively, and appropriate magnetic and mechanical boundary conditions. In the software, the MSS method uses the boundary condition

$$\mathbf{n}(\boldsymbol{\sigma}_2 - \boldsymbol{\sigma}_1) = 0, \quad (7)$$

where  $\mathbf{n}$  is the normal to the surface bounding magnetic and non-magnetic domains,  $\boldsymbol{\sigma}_2$  is the stress tensor at the interface corresponding to the air domain, and  $\boldsymbol{\sigma}_1$  is the stress tensor at the interface corresponding to the MAE domain. The stress tensors can be determined from

$$\boldsymbol{\sigma}_1 = \boldsymbol{\sigma} + \boldsymbol{\sigma}_H, \quad (8)$$

$$\boldsymbol{\sigma}_2 = \boldsymbol{\sigma}_H, \quad (9)$$

where the air domain (subscript 2) contains only the magnetic component and the MAE (subscript 1) inherently contains the magnetic and elastic components. The components of the magnetic stress tensor are given by [44].

$$\boldsymbol{\sigma}_H = \frac{1}{\mu_0} (B_i B_j - 0.5 \delta_{ij} B_i B_j), \quad (10)$$

where  $\boldsymbol{\sigma}_H$  is the magnetic component of the Maxwell stress tensor (which can differ in domains 1 and 2). Substituting (8)–(10) into (7) yields an additional condition that couples the solution of the induction field to that of the displacement field, through deformation of the boundary, requiring iterative solution [14]. The Maxwell stress tensor is also used in other numerical formulations for soft-magnetic MAE materials [44, 45] and is similar to the method proposed in [43].

*Boundary conditions.* As seen in figures 2, 3 and 4, the displacement boundary conditions for the three structures vary. The cantilever beam is subjected to a fixed boundary condition on the bottom portion of the sample; the two-segment accordion structure is subjected to fixed boundary conditions on the top and bottom boundaries of the substrate; the four-segment accordion structure is subjected to a fixed boundary condition on the top boundary of the substrate.

For all three structures, the perfect magnetic conductor boundary condition was applied to the upper and lower boundaries of the air domain. This is a special case of a surface current boundary condition that sets the tangential component of the magnetic field to zero [16]. As a result, the surface current density is also set to zero. This boundary



**Table 2.** Effective material properties for the cantilever beam, two-segment, and four-segment accordion structures along with range of field strengths the structures were subjected to.

|                              | Cantilever beam | Two-segment accordion | Four-segment accordion |
|------------------------------|-----------------|-----------------------|------------------------|
| Parameter                    | Value           | Value                 | Value                  |
| H (mT)                       | 0–40 mT         | 0–45                  | 0–200                  |
| M<br>(Amps m <sup>-1</sup> ) | 55 000          | 35 000                | 35 000                 |
| C <sub>10</sub>              | 300 000         | 63 000                | 63 000                 |
| C <sub>01</sub>              | 275 000         | 31 000                | 31 000                 |
| E <sub>MAE</sub> (Pa)        | —               | 1450 000              | 1450 000               |

conditions is given as

$$\mathbf{n} \times \mathbf{H} = \mathbf{0}. \quad (11)$$

Also, a magnetic potential boundary condition as applied to the left and right boundaries of the air domain. This boundary condition is given as

$$\mathbf{n} \times \mathbf{A} = \mathbf{n} \times \mathbf{A}_0, \quad (12)$$

where  $\mathbf{A}$  and  $\mathbf{A}_0$  are the magnetic vector potentials applied to the left and right boundaries, respectively, of the air domain in the models. Varying the values of  $\mathbf{A}$  and  $\mathbf{A}_0$  allow for changes to the simulated applied magnetic field.

In the simulations, the magnetic induction is applied through the magnetic vector potential  $\mathbf{A}$  via

$$\mathbf{B} = \nabla \times \mathbf{A}. \quad (13)$$

Equations (1b), (1c), (2) and (7), along with appropriate magnetic boundary conditions, can then be used to generate a system of equations in the vector field  $\mathbf{A}$  for solution of the magnetic induction.

Across all domains continuity in the magnetic vector potential,  $\mathbf{A}$ , is enforced. Across MAE and PDMS boundaries only, continuity in the displacement field,  $\mathbf{u}$ , is enforced. The independent variables used in the models can be seen in table 2.

**Effective material properties.** Solution of the model requires values for the elastic and magnetic constants. For the cantilever geometry, the elastic constants for the Mooney–Rivlin model,  $C_{01}$  and  $C_{10}$ , were determined by fitting finite element simulation data to experimental data representing purely elastic response, e.g. the bottom curve for  $\mathbf{H}=\mathbf{0}$  in figure 7. The value for  $M$ , the magnitude of the magnetization, for the cantilever geometry was determined by best fit of the simulation, given the previously determined elastic constants, to the experimental data at zero-displacement (along the  $y$ -axis in figure 7) to model a primarily magnetically driven response. For the two- and four-segment accordion geometries, purely elastic data were unavailable from the performed experiments therefore the elastic constants were determined by separate tensile tests on

samples of the MAE and PDMS substrate materials with a Shimpo screw-driven load stand at quasi-static strain rates. Similar to the cantilever geometry, the value for  $M$  for the two-segment geometry was found by best fit to the experimental data for reaction force; the same value was used for the four-segment geometry since it used nominally the same MAE material. The magnetization directions with respect to structure are as shown in figures 2–4 and were applied in an Eulerian frame. The materials properties are summarized in table 2.

**Finite element formulation.** The finite element formulation of a problem in Comsol Multiphysics is detailed in [41] and is briefly summarized here. Comsol Multiphysics seeks to solve the above defined set of governing differential and algebraic constraint equations across the discretized domains of the modeled structures. An automated mesh-generation routine defines the mesh with proscribed local refinements within a globally proscribed mesh size tolerance. The governing differential equations are then taken from the strong form and converted into their weak form allowing implementation of the Galerkin method. The program approximates the dependent variables using a linear combination of basis functions and a vector representation of the degrees of freedom in the model which can be expressed as:

$$u_l = \sum_i U_i \varphi_i^{(l)}, \quad (14)$$

where  $u_l$  is the piecewise continuous  $l$ th dependent variable (e.g.  $u, v$ , or  $w$ ),  $\mathbf{U}$  is the discrete elemental solution vector with degrees of freedom  $U_i$  as its components, and  $\varphi_i$  are the basis functions for the dependent variables [41]. Quadratic basis functions were used in these simulations.

Since the boundary and other conditions such as equation (7) are dependent upon  $\mathbf{U}$ , a set of constraint equations,  $\mathbf{M}_c$ , may be added to the governing system and written in a compact form

$$\mathbf{0} = \mathbf{M}_c(\mathbf{U}). \quad (15)$$

After constraints are applied, completing the set of equations, the program attempts to solve the system iteratively. Note that for this work the problems are considered two-dimensional and are solved in the Eulerian frame using large deformation kinematics as well as moving- and adaptive-mesh features which aid solution at large deformations and/or in regions with large gradients in the solution variables.

#### Mesh convergence

The FEA for the cantilever, two-segment, and four-segment geometries employed both a mesh convergence study to determine a sufficient value of degree of freedom density in each model as well as a convergence study on the size of the bounding air box needed to model the application of the magnetic field. Converged meshes for all three cases are shown in figures 5(a)–(c). In each case a sufficient number

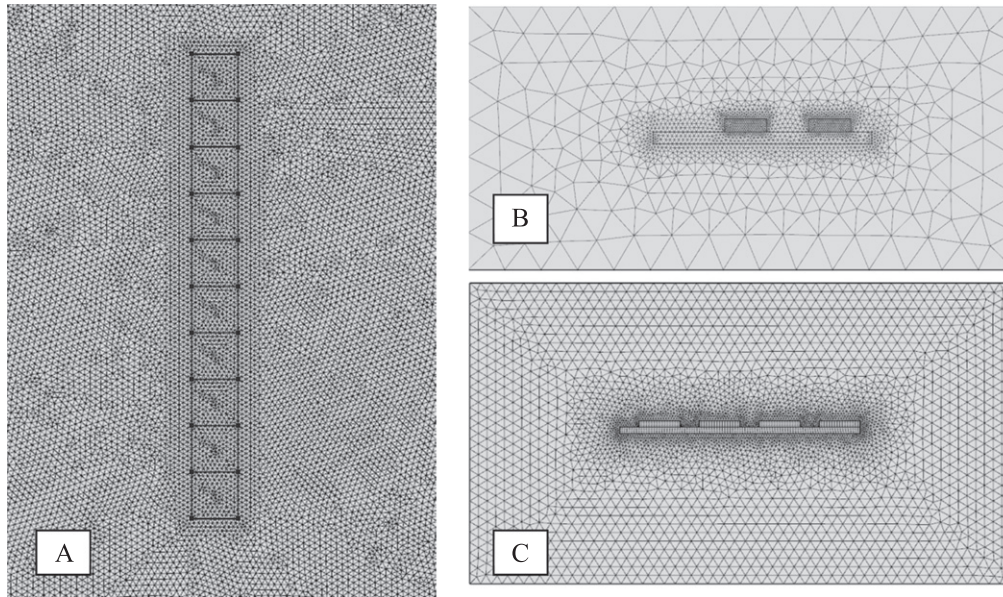


**Figure 5.** A view of the (a) cantilever, (b) two-segment accordion and (c) four-segment accordion structures' meshes showing local refinements and extent of the bounding air box. Relative sizes across figures are not to scale.

**Table 3** Converged, average, degree of freedom densities and the bounding box size ratios where the variables B, D,  $G'$ ,  $F'$ ,  $G''$ , and  $F''$  can be found in figure 1.

|   | DoF density<br>(DoF mm <sup>-2</sup> ) | Bounding box size<br>ratio ( $x, y$ ) |
|---|--|---------------------------------------|
| Cantilever beam                           | 11.1                                   | (16B, 2D)                             |
| Two-segment accordion                     | 14.2                                   | (4 $G'$ , 16 $F'$ )                   |
| Four-segment accordion<br>triangular mesh | 12.9                                   | (4 $G''$ , 16 $F''$ )                 |
| Four-segment accordion<br>Quad mesh       | —                                      | —                                     |
| Quad mesh                                 | 11.7                                   | (4 $G''$ , 16 $F''$ )                 |

of elements and size of the bounding box was used to ensure both uniformity in the magnetic field at the boundaries (the far field) and convergence of the reaction forces (cantilever and two-segment accordion) or average bend angle (four-segment accordion) models. The converged, average, degree of freedom densities and bounding box size ratios (maximum model dimension to box dimension in either the  $x$  or  $y$  dimension) are given in table 3. Note that meshes were refined at locations where the solution was expected to vary sharply relative to other areas. The cantilever and two-segment accordion structure were modeled with triangular elements of quadratic order and periodically remeshed to retain mesh quality. Two separate mesh geometries were analyzed for the four-segment accordion geometry. First attempts used quadratic, triangular elements and remeshing as in the cantilever and four-segment geometries. A second method used quadratic, quadrilateral elements (without remeshing). Both methods yielded similar results.

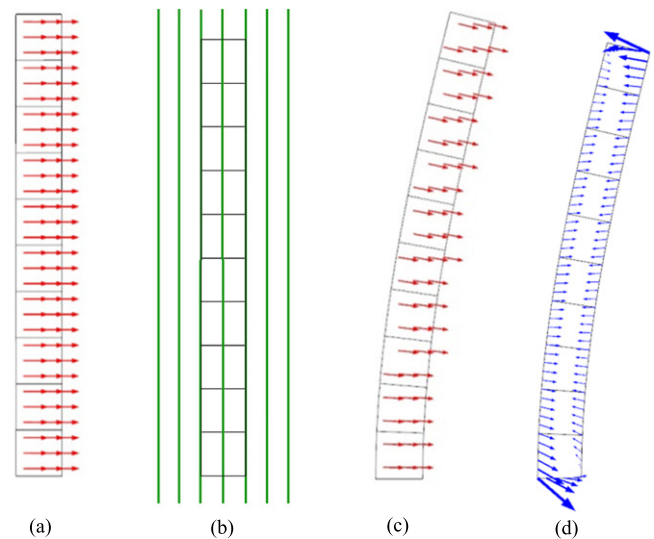


**Figure 6.** Results of simulations of the (a) remanent magnetization in red arrows, (b) magnetic field in red streamlines, (c) remanent magnetization in red arrows for the cantilever deformed geometry and (d) Maxwell surface tractions in blue arrows for the cantilever deformed geometry.

## Results

### Cantilever beam simulations

For a typical cantilever simulation, the remanent magnetization, magnetic flux streamlines, remanent magnetization in the deformed geometry, and the MSS vectors in the deformed geometry can be seen in figure 6. The remanent magnetization vectors are displacing with the structure as it actuates (figure 6(c)), the calculated Maxwell tractions act in a manner such that the resulting torque acts counter-clockwise (as expected from the direction of the magnetization and upward

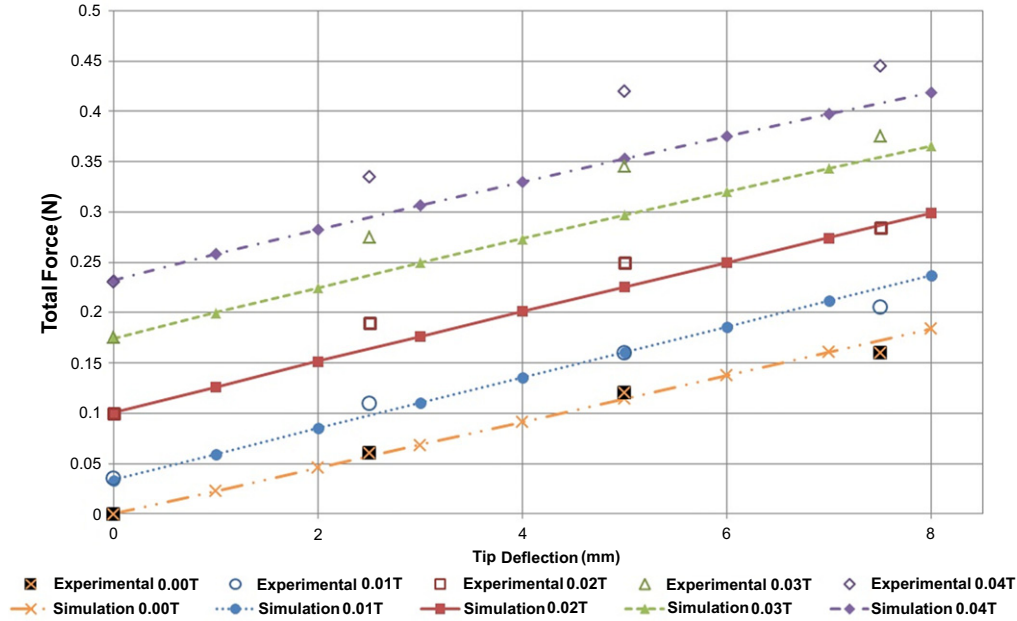


**Figure 7.** Comparison of experimental data (points) [3] to finite element simulations (lines-points) for the cantilever geometry.

direction of the external field), and the magnetic field lines are running in the prescribed direction. Simulation results of resultant tip force versus displacement for varying applied fields are shown and compared to experimental data from the literature [3] in figure 7. The tip force is taken from the total  $x$ -direction reaction force across the top boundary where the  $x$ -displacements are proscribed.

The measured total load  $F_T$  reflected the combined result of the elastic  $F_e$  and magnetic  $F_H$  responses, i.e. where the magnetic behavior was a function of applied field  $H$  and tip displacement  $\delta$  while the elastic response was considered a function of  $\delta$  only, see equation (1).

$$F_T(H, \delta) = F_H(H, \delta) + F_e(\delta). \quad (16)$$

The zero-field measurements yielded the elastic forces,  $F_T(0, \delta) = F_e(\delta)$  (figure 7) and were consequently used to characterize the elastic response by fitting the finite element model solution to experimental data by best fit of hyperelastic material parameters  $C_{10}$  and  $C_{01}$  in the simulation. The zero-displacement, e.g. blocked force, measurements (figure 7 along the  $y$ -axis) yielded the magnetic forces  $F_T(H, 0) = F_H(H)$ , devoid of elastic forces (those causing macroscopic deformation) since the macroscopic geometry was undeformed. The magnetic force measurements were used to characterize the magnetic response by fitting the model solution for  $F_H$  to experimental data by best fit of the magnetization,  $\|\mathbf{M}\| = M$ , to an effective value, which was assumed constant and aligned transverse to the beam axis, used in simulations.

Predicted results show good agreement over a range of intermediate field strengths and displacement values especially given that no constants were adjusted to fit these intermediate data. Variations may be due to inadequate restriction of the magnetic particles within the matrix thus allowing rotation of the particles without actuation of the

cantilever, assuming a uniform magnetization when a distribution of magnetization orientations is expected across the particles, assuming a fixed magnetization when the value may change with applied field, or possible boundary effects in the experiment.

#### Two-segment accordion simulations

A typical simulation for the two-segment accordion structure applies a magnetization to the MAE specimens, applies a magnetic flux, and actuates through the MSS vectors shown in figures 8(a), (b), and (c) respectively. Note that the tractions seen in figure 8(c) produce a net torque that creates the mountain fold. This is to be expected as the magnetic field is constant, but the  $y$ -component of the magnetization for the top MAE patch is opposite of the magnetization of the bottom MAE patch. From  $\mathbf{T} = \mathbf{M} \times \mathbf{H}$ , one can see that the torques should be opposing one another.

Simulations used the Mooney–Rivlin strain energy density to model the PDMS substrate where the  $C_{01}$  and  $C_{10}$  parameters were determined by matching simulation data to separate experimental quasi-static tensile-test data (not shown). The modulus of the MAE samples was also taken from experimental quasi-static tensile test data which showed linear behavior of the observed range of strains in the MAE domains (not shown).

The simulation and experimental results can be seen in figure 9 for the (a) observed bend angle of the structure and (b) resultant force measured at the proscribed displacement node of the PDMS substrate. The bend angle and resultant force that were measured are shown in figure 3(b). For moderate fields ranging from 0 to 40 mT, the resultant tip force, shown in figure 9(a), is accurately predicted by the finite element model while the bend angle differs by a maximum of only 3%.



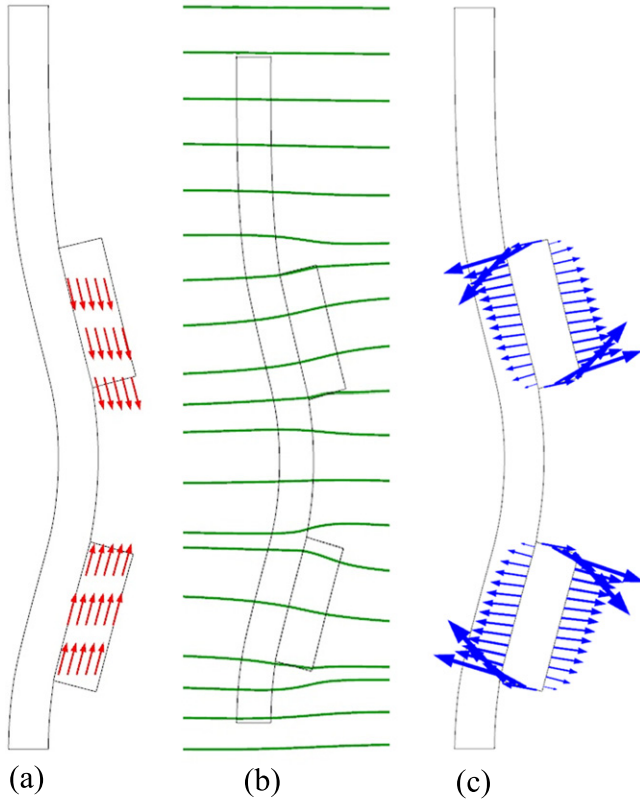


**Figure 8.** Simulation results of the (a) remanent magnetizations of the MAE segments in red arrows, (b) the magnetic flux, in green streamlines, and (c) of Maxwell surface stress tensor for the two-segment accordion structure with the relative size of the tractions depicted in blue arrows. Note the traction would produce opposing torques on the MAE patches due to their opposing remanent magnetizations.

Differences between observed bend angles in the simulation and experiment may be attributed to over-stiffening of the PDMS substrate within the finite element model. Also, the effective magnetization used in the model was chosen by fitting the simulation data to experimental data through parametric sweeps of the applied magnetization. While this effective magnetization models the axial force exerted by the structure under the application of an external field well, it may not accurately describe the magnetization of MAE specimens and hence affect predicted deformation which can be more dependent on the distribution of the magnetization as opposed to its bulk behavior.

#### Four-segment accordion simulations

A typical simulation for the four-segment accordion structure applies the proscribed magnetization to the MAE specimens, applies an increasing magnetic flux, and actuates through the MSS vectors shown in figures 10(a), (b), and (c) respectively. Note that the tractions seen on the MAE domains in figure 10(c) should produce torques whose net response alternates in sign from patch to patch to create the mountain-valley fold structure. This is to be expected as the applied magnetic field is constant but the internal magnetizations of MAE patches alternate. The figure, however, depicts that the

long ends of the MAE patches work in opposition to the short ends of the MAE patches.

Simulations used the same elastic and magnetic parameters as those in the two-segment accordion structure. The simulation (for triangular elements) and experimental results [6] can be seen in figure 11 for the observed bend angles of the structure. The bend angles that were measured are shown in figure 4(b) and the data shown in figure 11 are the average of the two measured angles.

The results presented in figure 11 show similar trends between the finite element model and the experimental data (i.e. asymptotic behavior of the bend angle as the magnetic field increases in magnitude) but diverge as magnetic field increases. It was observed in the simulations that increasing the effective magnetization or decreasing the elastic stiffness parameters in the four-segment finite element model did not affect the maximum bend angle; the asymptote remained the same. This suggests over-stiffening (numerical locking) of the structure. Although adaptive remeshing and triangular and quadrilateral element geometries were used, the locking phenomena remained.

#### MEK simulation

A MEK model was used to model the four-segment accordion geometry to circumvent possible numerical locking phenomena at large deformation in the finite element model. This method assumed the MAE patches and the substrate to which they were attached acted as rigid links between the more compliant sections of the PDMS substrate only. These PDMS substrate only sections were assumed to act as torsional springs with bending stiffness

$$k = \frac{EI}{L}, \quad (17)$$

where  $I$  is the second moment of inertia of the substrate domain,  $L$  is the length of the PDMS substrate only section, and  $E$  is the elastic modulus of the substrate. These assumptions are warranted given the difference in elastic stiffness between the two materials and upon observation that the MAE patches did not bend noticeably relative to the PDMS substrate. For the boundary connection to the fixed end, a length  $L/2$  is used.

The MEK model of the accordion seeks to minimize the combined Zeeman magnetic energy (*sans* demagnetizing fields) of the MAE patches coupled with a linear torsional spring energy that represents the elasticity of the fold. The energy functional of the model is given as

$$\Pi(\theta) = \sum_{i=1}^4 \left[ -\frac{1}{2} \mu_0 \mathbf{m}_i \cdot \mathbf{H} + \frac{1}{2} k_i (\theta_i - \theta_{i-1})^2 \right], \quad (18)$$

where  $\theta = \{\theta_0, \dots, \theta_4\}$ ,  $\mu_0$  is the magnetic permeability of free space,  $k$  is the torsional spring constant,  $\theta_i$  is the angle the MAE patch makes with the horizontal (with  $\theta_0 = 0$  representing the fixed boundary),  $\mathbf{H} = [0, H]^T$ , where  $H$  is the

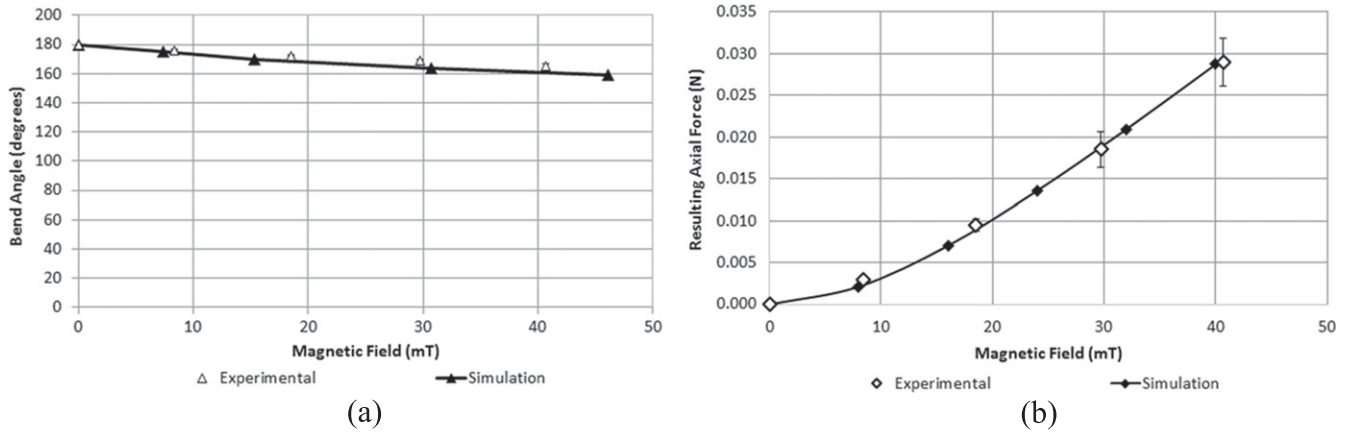


**Figure 9.** Comparison of the experimental (open symbol) and FEA results (solid symbols) of the (a) observed bend angle and (b) reaction force versus applied magnetic fields ranging from 0 to 40 mT.

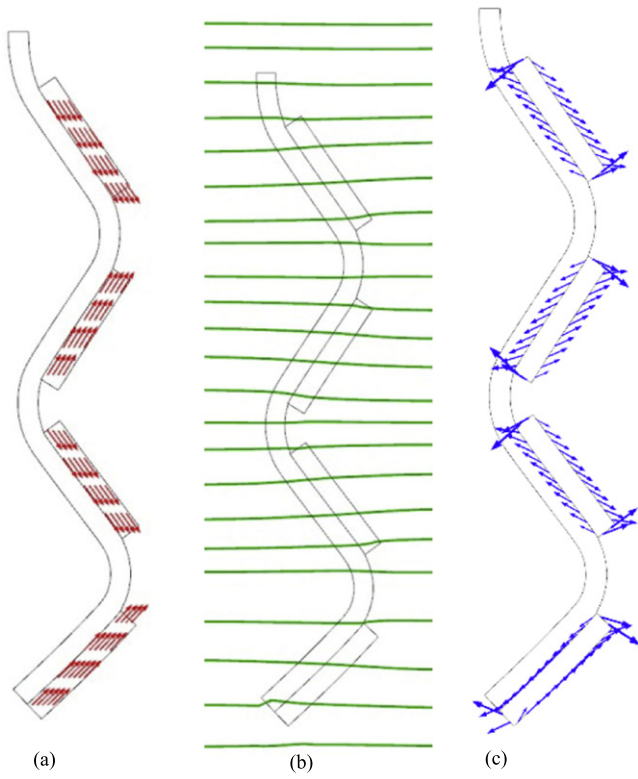


**Figure 10.** Depiction of the (a) remanent magnetizations of the MAE segments in red arrows, (b) magnetic flux, in green streamlines, and the (c) Maxwell surface stress vectors for the four-segment accordion structure with the relative size of the tractions depicted in blue arrows. Note the traction would produce opposing torques on the MAE patches.

applied field and

$$\mathbf{m}_i = V_i M_i \left[ (-1)^{i-1} \cos \theta_i, \sin \theta_i \right] \quad (19)$$

is the magnetic moment of the  $i$ th MAE patch, having north poles oriented in an alternating fashion as shown, and  $V_i$  as the volume of the  $i$ th MAE patch, respectively (see figure 12). Gravity is not considered in this model.

Magnetization values were taken directly from magnetization experiments that determined  $\mu_0 M \approx 75.4$  mT (not

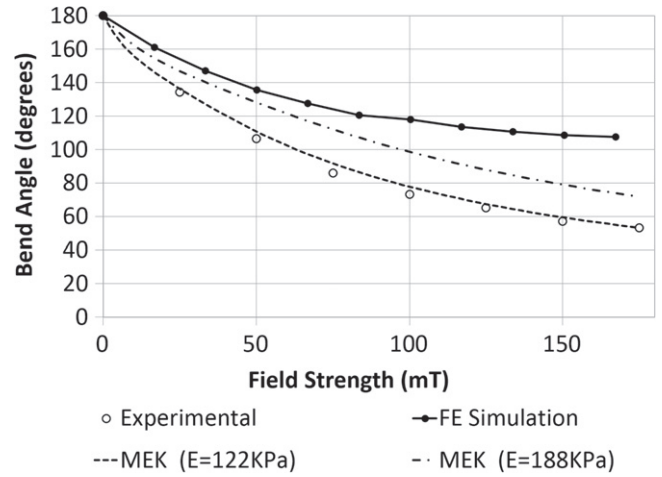


**Figure 11.** Comparison of experimental (open circle), finite element simulation (filled-circle, black lines), and minimum energy kinematic simulations with best-fit modulus (dotted line) and actual modulus (dashed-dotted line) results for the four-segment accordion structure where average bend angles of the structure are observed as a function of the magnetic field.

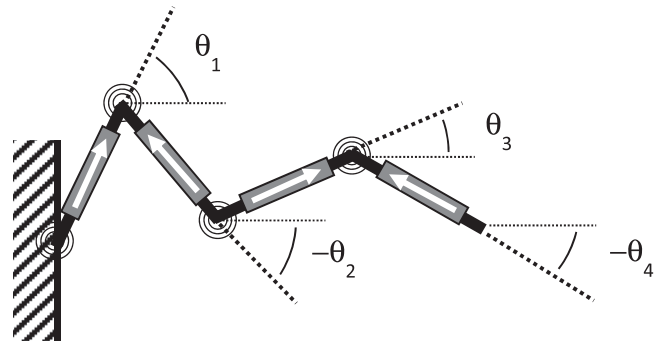


**Figure 12.** Schematic of kinematic model for use with the MEK method. The figure shows bend angles with respect to the horizontal,  $\theta_i$  and MAE patches with magnetization orientation shown by white arrows.



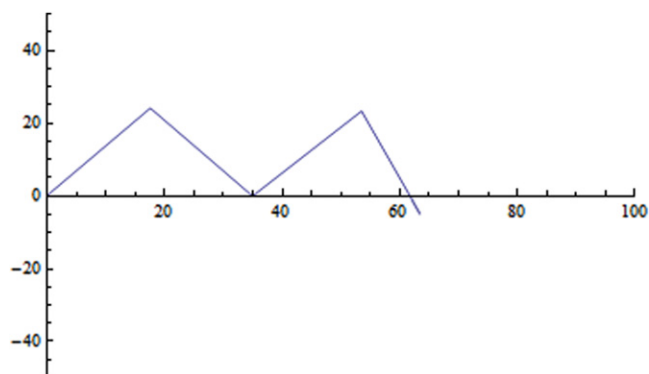


**Figure 13.** Representative deformed configuration for the four-segment accordion structure using the MEK.

shown). The modulus  $E \approx 188$  kPa was derived from small strain approximations to the Mooney–Rivlin constants used in the previous two- and four-segment accordion finite element simulation.

Fixed boundary conditions were enforced by setting  $\theta_0 = 0$  at the fixed end. The solution of the MEK model requires

$$\frac{\partial \Pi}{\partial \theta_i} = 0 \quad \forall i = 1 \dots 4, \quad (20)$$

yielding solutions for the four orientation angles, and thereby the fold angles. The method does not require solution of the local flux density and therefore requires no air box.

A representative deformed configuration is shown in figure 13. Average fold angle results using the MEK simulations are also compared to the finite element model which used the MSS method and to the experimental data, (figure 11). Two MEK simulation results are shown. The dashed line represents the best fit achieved by choosing  $E = 122$  kPa to fit the final data point at  $\mu_0 H = 0.175$  mT. The dashed-dotted line uses  $E = 188$  kPa as found from the experimental tensile tests and used, in an equivalent form, in the Mooney–Rivlin constants for the finite element simulations.

The MKS simulations were not limited in terms of maximum achievable fold angle. The best-fit simulation, while using measured values for all other parameters, showed excellent agreement with the data using a modulus reduced by 35%; the actual modulus returns an overly stiff response. The required reduction in modulus could stem from several factors including demagnetizing fields and a lack of cohesion between the particles and the matrix.

## Conclusions

This work studied the behavior of MAEs and MAE composite structures under the application of magnetic fields. These MAE materials and structures were actuated via a magnetic torque acting either on a monolithic MAE cantilever geometry, or on multiple MAE patches attached to a PDMS substrate. The geometries studied were chosen to represent

the basis for bending and subsequently folding behaviors that are the basis for creating mountain-valley conformations which are central to origami folding techniques.

Experimental behavior was compared to finite-element models constructed with Comsol Multiphysics in which the MSS method was used to couple the hyper-elastic and magnetic responses. Finite element simulations of the four-segment accordion, however, were prone to numerical locking having undetermined elastic or magnetic origins. Consequently, a MEK model of the four-segment accordion was developed that assumed linear-elastic torsional springs separated by rigid links subject to a Zeeman magnetic energy potential. Using parameters taken nearly entirely from direct measurements, the MEK simulations showed excellent agreement to experimental data for a ‘best-fit’ elastic modulus (the sole adjustable parameter) of roughly 65% of the measured value. The difference between model constants used and actual measured values may find roots in a host of factors including insufficient restriction of the magnetic particles in the matrix (i.e. particles may be able to rotate under the application of a magnetic field without actuation in the bulk), a distribution of the magnetization orientation about the nominal magnetizing axis, non-uniform fields in the test geometry and demagnetizing fields.

The work has illustrated the efficacy of the MSS method at low fields and for simpler models to accurately predict MAE and MAE composite response. The MEK method was further shown effective at predicting large deformation behavior. The methods presented in this paper have improved upon previous works modeling magneto-elastic composites by outlining a means for incorporating hard-magnetic behavior, specifically magnetic torque generation, and coupling it with elastic response at large deformations. While future work is still needed to employ constituent-based material response models, and hence material descriptions that allow material behavior to be predicted directly from composition, this work highlights how use of effective properties allows future researchers to design and investigate origami structures with different geometries and boundary conditions.

## Acknowledgments

The authors gratefully acknowledge the support of the National Science Foundation (NSF) EFRI grant number 1240459, NSF CMMI grant number 0927326, and AFOSR. Any opinions, findings, and conclusions or recommendations expressed in this material are those of the authors and do not necessarily reflect the views of the National Science Foundation.

## References

- [1] Du G and Chen X 2012 MEMS magnetometer based on magnetorheological elastomer *Measurement* **45** 54–8
- [2] Farshad M and Benine A 2004 Magnetoactive elastomer composites *Polym. Test.* **23** 347–53

- [3] von Lockette P *et al* 2011 Investigating new symmetry classes in magnetorheological elastomers: cantilever bending behavior *Smart Mater. Struct.* **20** 105022
- [4] Koo J-H, Dawson A and Jung H-J 2012 Characterization of actuation properties of magnetorheological elastomers with embedded hard magnetic particles *J. Intell. Mater. Syst. Struct.* **23** 1049–54
- [5] Stepanov G V, Chertovich A V and Kramarenko E Y 2012 Magnetorheological and deformation properties of magnetically controlled elastomers with hard magnetic filler *J. Magn. Magn. Mater.* **324** 3448–51
- [6] von Lockette P and Sheridan R 2013 Folding actuation and locomotion of novel magneto-active elastomer (MAE) composites *Proc. of the 2013 Smart Materials, Adaptive Structures, and Intelligent Systems Conf.* (Snowbird, Utah) SMASIS2013-3222
- [7] von Lockette P R and Lofland S 2011 Role of magnetization anisotropy in the active behavior of magnetorheological elastomers *Proc. of the 2011 Smart Materials, Adaptive Structures, and Intelligent Systems Conf.* (Scottsdale, AZ) SMASIS2011-5115
- [8] Zhou G Y 2003 Shear properties of a magnetorheological elastomer *Smart Mater. Struct.* **12** 139–46
- [9] Nayak B, Dwivedy S K and Murthy K 2013 Dynamic stability of magnetorheological elastomer based adaptive sandwich beam with conductive skins using FEM and the harmonic balance method *Int. J. Mech. Sci.* **77** 205–16
- [10] Shen Y, Golnaraghi M F and Heppler G R 2004 Experimental research and modeling of magnetorheological elastomers *J. Intell. Mater. Syst. Struct.* **15** 27–35
- [11] Lokander M and Stenberg B 2003 Improving the magnetorheological effect in isotropic magnetorheological rubber materials *Polym. Test.* **22** 677–80
- [12] Lokander M and Stenberg B 2003 Performance of isotropic magnetorheological rubber materials *Polym. Test.* **22** 245–51
- [13] von Lockette P R, Lofland S E, Koo J H, Kadlowec J and Dermond M 2008 Dynamic characterization of bimodal particle mixtures in silicone rubber magnetorheological materials *Polym. Test.* **27** 931–5
- [14] Inoue M, Levy M and Baryshev A V 2013 *Magnetophotonics: From Theory to Applications* (Heidelberg: Springer)
- [15] Stoll A, Mayer M, Monkman G and Shamonin M 2014 Evaluation of highly compliant magneto-active elastomers with colossal magnetorheological response *J. Appl. Polym. Sci.* **131** 39793
- [16] Comsol 2010 *Comsol Multiphysics's User Guide*, Comsol AB
- [17] Barham M, White D and Steigmann D 2010 Finite element modeling of the deformation of magnetoelastic film *J. Comput. Phys.* **229** 6193–207
- [18] Bustamante R, Dorfmann A and Ogden R W 2011 Numerical solution of finite element geometry boundary-value problems in nonlinear magnetoelasticity *Int. J. Solids Struct.* **48** 874–83
- [19] Martinez R V, Fish C R, Chen X and Whitesides G M 2012 Elastomeric origami: programmable paper-elastomer composites as pneumatic actuators *Adv. Funct. Mater.* **22** 1376–84
- [20] Okuzaki H, Saido T, Suzuki H, Hara Y and Yan H 2008 A biomorphic origami actuator fabricated by folding a conducting paper *J. Phys.: Conf. Ser.* **127** 012001
- [21] Firouzeh A *et al* 2013 Sensor and actuator integrated low-profile robotic origami *The Int. Conf. on Intelligent Robots and Systems* (Tokyo, Japan) 3–7 November
- [22] Paik J *et al* 2011 Stretchable circuits and sensors for robotic origami *The Int. Conf. on Intelligent Robots and Systems* (San Francisco, CA) 25–30 September
- [23] Borcea L and Bruno O 2001 On the magneto-elastic properties of elastomer-ferromagnet composites *J. Mech. Phys. Solids* **49** 2877–919
- [24] Dorfmann A and Ogden R 2003 Magnetoelastic modelling of elastomers *Eur. J. Mech. A* **22** 497–507
- [25] Kankanala S and Triantafyllidis N 2004 On finitely strained magnetorheological elastomers *J. Mech. Phys. Solids* **52** 2869–908
- [26] Yin H, Sun L and Chen J 2002 Micromechanics-based hyperelastic constitutive modeling of magnetostrictive particle-filled elastomers *Mech. Mater.* **34** 505–16
- [27] Coquelle E 2006 Micromechanical analysis of an elastomer filled with particles organized in chain-like structure *J. Mater. Sci.* **41** 5941–53
- [28] Ponte Castañeda P and Galipeau E 2011 Homogenization-based constitutive models for magnetorheological elastomers at finite strain *J. Mech. Phys. Solids* **59** 194–215
- [29] Tuan H and Marvalova. B 2010 *Magnetoelastic Anisotropic Elastomers in a Static Magnetic Field: Constitutive Equations and Fem Solutions* (London, UK: Taylor & Francis Group)
- [30] Galipeau E and Ponte Castañeda P 2012 The effect of particle shape and distribution on the macroscopic behavior of magnetoelastic composites *Int. J. Solids Struct.* **49** 1–17
- [31] Galipeau E and Ponte Castañeda P 2013 A finite-strain constitutive model for magnetorheological elastomers: magnetic torques and fiber rotations *J. Mech. Phys. Solids* **61** 1065–90
- [32] von Lockette P 2012 Novel actuation mechanisms in magnetorheological materials *Smart Materials, Adaptive Structures, and Intelligent Systems Conf.* (Stone Mountain, Georgia) p 8143
- [33] Dorfmann A and Brigadnov I A 2003 Constitutive modeling of magneto-sensitive Cauchy-elastic solids *Comput. Mater. Sci.* **29** 270–82
- [34] Bustamante R, Dorfmann A and Ogden R W 2007 Nonlinear magnetoelasticity *J. Eng. Math.* **59** 139–53
- [35] Vogel F, Bustamante R and Steinmann P 2013 On some mixed variational principles in magneto-elastostatics *Int. J. Nonlinear Mech.* **51** 157–69
- [36] Dorfmann A and Ogden R W 2004 Nonlinear magnetoelastic deformations *Q. J. Mech. Appl. Math.* **57** 599–622
- [37] Bustamante R, Dorfmann A and Ogden R W 2009 On electric body forces and Maxwell stresses in nonlinearly electroelastic solids *Int. J. Eng. Sci.* **47** 1131–41
- [38] Barham M, Steigmann D J and White D 2012 Magnetoelasticity of highly deformable thin films: theory and simulation *Int. J. Nonlinear Mech.* **47** 185–96
- [39] Kim B *et al* 2012 A comparison among Neo-Hookean model, Mooney–Rivlin model, and Ogden model for chloroprene rubber *Int. J. Precis. Eng. Manuf.* **13** 759–64
- [40] Bower A F 2012 *Applied Mechanics of Solids* 1st edn (Boca Raton, FL: CRC Press)
- [41] Multiphysics C 2012 *Comsol Multiphysics Reference Guide COMSOL* (Stockholm, Sweden) May pp 563–4
- [42] Raikher Y L, Stolbov O V and Stepanov G V 2008 Shape instability of a magnetic elastomer membrane *J. Phys. D: Appl. Phys.* **41** 152002
- [43] Raikher Y L and Stolbov O V 2005 Deformation of an ellipsoidal ferrogel in a sample in a uniform magnetic field *J. Appl. Mech. Tech. Phys.* **46** 434–43
- [44] Hoffman T J and Chudzicka-Adamczak M 2009 The Maxwell stress tensor for magnetoelastic materials *Int. J. Eng. Sci.* **47** 735–9
- [45] Vogel F, Bustamante R and Steinmann P 2013 On some mixed variational principles in magneto-elastostatics *Int. J. Nonlinear Mech.* **51** 157–69